Chalcogenide Letters

Tech Science Press

http://doi.org/10.32604/cl.2026.079721

ARTICLE

Self-Assembled MoS_2/Graphene Oxide Hybrid Structures for High-Capacity Supercapacitors: A Scalable Approach

Mohsin Sayeed[1,*], O. P. Singh[1], Vishal Singh Chandel[2], Azam Raza[3], Kamal Batcha Mohamed Ismail[4], Mayur Khan[5], Navshad Alam[6,7] and Mohammad Shariq[8]

[1]Department of Applied Science and Humanities, Institute of Engineering and Technology, Lucknow, Uttar Pradesh, India
[2]Department of Applied Science and Humanities, Rajkiya Engineering College, Ambedkar Nagar, Uttar Pradesh, India
[3]Interdisciplinary Nanotechnology Centre (INC), Zakir Husain College of Engineering & Technology (ZHCET), Aligarh Muslim University, Aligarh, Uttar Pradesh, India
[4]Department of Electronics and Communication Engineering, Agni College of Technology, Chennai, Tamil Nadu, India
[5]Nuclear Physics Institute of Czech Academy of Sciences, Řež 130, Husinec, Czech Republic
[6]United College of Engineering and Research, Naini, Prayagraj, India
[7]Department of Applied Science and Humanities, SR Institute of Management and Technology, Lucknow, Uttar Pradesh, India
[8]Department of Physical Sciences, Physics Division, College of Science, Jazan University, Jazan, Saudi Arabia
*Corresponding Author: Mohsin Sayeed. Email: syedmohsinsayeed@gmail.com

Received: 13 February 2026; Accepted: 22 April 2026; Published: 09 May 2026

ABSTRACT: An eco-friendly one-pot hydrothermal method was developed to synthesize molybdenum disulfide/graphene oxide (MoS_2/GO) nanocomposites for high-performance supercapacitor applications. X-ray diffraction (XRD) analysis confirmed the presence of the MoS_2 crystalline phase, with reduced peak intensities upon GO incorporation, indicating suppressed crystallite growth. Scanning electron microscopy (SEM) revealed rod-like MoS_2 structures uniformly distributed across layered GO sheets, and energy-dispersive spectroscopy (EDS) confirmed the presence of Mo, S, C, and O elements. Raman and FTIR analyses verified strong interfacial interactions between MoS_2 and GO. Brunauer–Emmett–Teller (BET) measurements revealed a mesoporous structure with a specific surface area of ~31.7 m^2 g^{-1} and a pore size centered at ~4 nm, facilitating efficient ion transport. Electrochemical performance evaluated using cyclic voltammetry (CV) in 2 M KOH electrolyte demonstrated a high specific capacitance of 185 F g^{-1} at 5 mV s^{-1}. The quasi-rectangular CV curves and symmetric charge–discharge profiles indicate a combined electric double-layer and pseudocapacitive behavior. The MoS_2/GO composite also exhibited improved charge transfer properties and superior cycling stability over 10,000 cycles compared to pristine MoS_2. Density functional theory (DFT) calculations revealed that graphene oxide has a higher density of states near the Fermi level than MoS_2, indicating enhanced quantum capacitance and faster electron-transfer kinetics. The synergistic integration of MoS_2 and GO thus improves conductivity, structural stability, and electrochemical performance. These findings highlight the potential of MoS_2/GO nanocomposites as efficient electrode materials tailored for high-performance energy storage devices.

KEYWORDS: Hydrothermal; molybdenum disulfide; graphene oxide; cyclic voltammetry; DFT

1 Introduction

Climate change and the depletion of fossil fuel reserves have made the urgent need for clean and renewable energy sources more apparent. Simultaneously, technological advancements, particularly in devices such as smartphones, tablets, and digital cameras, have significantly enhanced modern life. As a result of these innovations, per capita energy consumption has increased substantially [1]. To address these challenges, researchers are increasingly focusing on low-cost and efficient energy storage solutions. Among these, electrochemical capacitors, commonly known as Supercapacitors, have garnered substantial attention owing to their outstanding properties, including excellent power density, rapid charge/discharge kinetics, long-lasting cycle performance, and minimal environmental impact [2]. These attributes position supercapacitors as promising candidates for meeting the growing global energy demand and accelerating the transition to sustainable energy sources. Additionally, nanostructured materials have attracted significant attention due to their outstanding mechanical, electrical, and optical properties [3]. Graphene is a unique carbon nanomaterial (1D, 2D, 3D) with exceptional potential for supercapacitor electrode applications, owing to its remarkable mechanical strength, outstanding conductivity, exceptional large surface area, and high chemical stability [4]. Recently, extensive research has been conducted on graphene-based metal sulfide composites for electrochemical energy storage, including In_3S_2/graphene, MoS_2/graphene, and NiS/graphene [5]. MoS_2, a transition-metal dichalcogenide, exhibits great promise due to its layered structure, consisting of a central molybdenum (Mo) intercalated within sulfur (S) layers and assembled by weak Van der Waals interactions [6,7]. Such strong electron-electron interactions in Mo atoms, combined with its unique layered structure, enhance planar electrical transport properties, making MoS_2 an excellent choice for functional applications [8]. MoS_2 composites integrated with carbonaceous conductors, e.g., MoS_2/graphene, MoS_2/carbon nanotubes, and MoS_2/mesoporous carbon, have been widely studied to improve their performance for various applications, including as anodes for LIBs, hydrogen evolution, and sensor technologies [9,10]. Using ammonium molybdate tetrahydrate and thiourea as precursors, we present an environmentally friendly, one-pot hydrothermal production of molybdenum disulfide/graphene oxide (MoS_2/GO) nanocomposites. For supercapacitor applications, the synthesized MoS_2/GO nanocomposite as an electrode material exhibits exceptional electrochemical performance, with a capacitance per unit mass of 185 F g^{-1} at a 5 mV/s scan rate, and excellent cycle stability. The findings emphasize the possibilities of MoS_2/GO composites designed for advancing next-generation energy storage devices.

2 Materials and Methods

Ammonium molybdate tetrahydrate ($(NH_4)_6Mo_7O_{24}\cdot 4H_2O$) (acquired from Sigma-Aldrich at 99.5% purity) and Thiourea (CH_4N_2S) (acquired at 98% purity from Alfa Aesar laboratory) were employed as precursors. Analytical-grade reagents and chemicals were acquired and employed directly, sans any additional purification.

3 Characterization Techniques

A Rigaku Miniflex Advance diffractometer (Cu Kα radiation, $\lambda = 1.541838$ Å) was employed to quantify the phase of crystallinity. Optics: For MoS_2 and MoS_2/GO, the 2θ angle range is 5.0° to 80.0° in 0.04° steps, and beta filtering is performed with graphite, an automated slit to control beam divergence, and a monochromator. SEM characterization was utilized to analyze the sample's morphology and identify its constituent elements via energy-dispersive X-ray spectroscopy (EDS) (Make-Japan, Model-JSM-6700 F) at an accelerating 10 kV potential. Fourier transform infrared (FTIR) spectroscopy (PerkinElmer) was used to identify functional biomolecules in the 400–4000 cm^{-1} range. For FTIR analysis, pellets were prepared by thoroughly mixing 2 mg of the synthesized nanomaterial with 200 mg of KBr, then compressing the mixture under high pressure. Raman spectra were recorded using a Renishaw RM-1000 Raman microscope equipped with a 50× objective and a 532 nm He–Ne laser as the excitation source.

3.1 Production of Graphene Oxide

The Hummers method, with modifications, was employed for GO synthesis [11], which involved oxidizing natural graphite powder (20 µm mesh, sourced from Sigma-Aldrich). Here, we present a modified version without $NaNO_3$. Usually, concentrated H_2SO_4 (30 mL) was mixed with graphite powder (1.0 g) while stirring in an ice-cooled bath to maintain the suspension temperature below 20°C. 4.0 g of $KMnO_4$ was added step by step (1 g at a 10-min interval) while vigorously stirring. Subsequently, the reactant mixture was immersed in a water bath at 40°C and quickly agitated for approximately sixty minutes. After adding 100 mL of double-distilled water, the solution was vigorously stirred for 45 min at 90°C. After adding another 300 mL of double-distilled water, 3 mL of hydrogen peroxide (30%) was gradually added, and the solution's color shifted from dark brown to yellow (filtrate). Then, by centrifugation, the filtrate was collected at 3000 rpm for 30 min, with the supernatant being decanted. The obtained solid material was washed successively with 150 mL of double-distilled water and 100 mL of 30% HCl. The supernatant was decanted and initially washed twice with 200 mL of ethanol, followed by three washes with 300 mL of double-distilled water each. The resulting solid was vacuum-dried at room temperature for eight hours.

3.2 Synthesis of MoS_2 Nanoparticles

Ammonium molybdate tetrahydrate ($(NH_4)_6Mo_7O_{24}{\cdot}4H_2O$), along with thiourea ($CH_4N_2S$), served as precursors for the synthesis of the nanoparticles of MoS_2. The first step involved mixing 4.48 g of thiourea with 0.70 g of the tetrahydrate form of ammonium molybdate $(NH_4)_6Mo_7O_{24}{\cdot}4H_2O$) in 70 mL of double-distilled water, stirring constantly until a clear solution was obtained. A black MoS_2 precipitate was removed at the end of treatment. Afterward, the resulting solution was transferred to a 100 mL Teflon-lined autoclave and heated to 180°C under 40 psi for 20 h. The obtained black precipitate was then thoroughly rinsed with ethanol and double-distilled water to lower the solution's pH to 3. Before being employed for additional examination, the precipitates were lastly dried for eight hours at 60°C.

3.3 Synthesis of MoS_2/GO Hybrid Nanocomposite

10 mg of GO was stirred into 50 mL of double-distilled water, along with 100 mg of MoS_2. The solution was ultrasonicated for 30 min; thereafter, it was transferred to a 100 mL autoclave with a stainless-steel body lined with Teflon and heated for 12 h at 180°C. Thus, the as-synthesized MoS_2–GO sample was obtained as shown in Fig. 1.

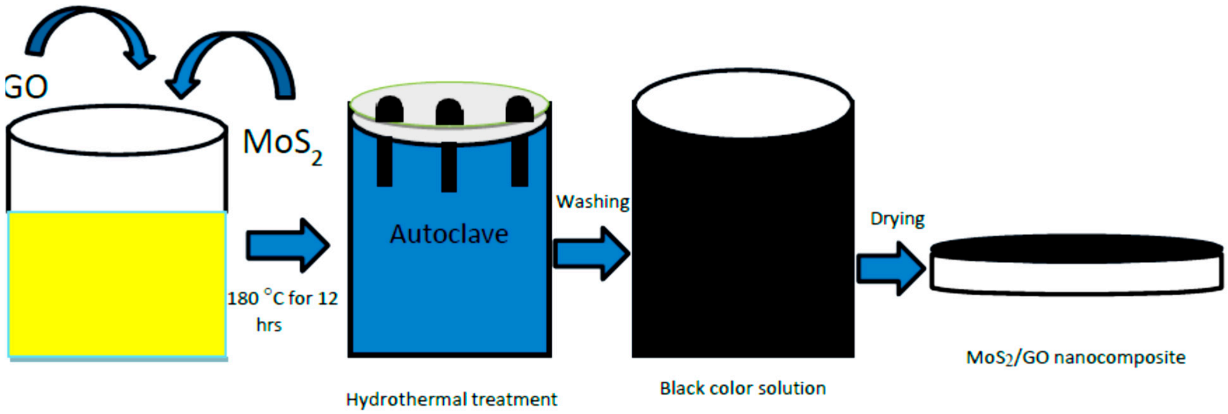

Figure 1: Schematic illustrating the hydrothermal synthesis of MoS_2/GO nanocomposites.

3.4 Electrode Preparation

A three-electrode cell configuration was employed for electrochemical impedance spectroscopy, chronopotentiometry, and cyclic voltammetry measurements. The working electrode material, activated carbon, and polyvinylidene fluoride (PVDF), combined at a weight ratio of 70:15:15, were well mixed using a mortar and pestle. 600 µL of N-methylpyrrolidone (NMP) was used as a solvent to transform the previously described mixture into a slurry. Activated carbon was used as a conductive filler, while PVDF was used as a binding agent. A 1 cm^2 graphite sheet was employed as the test electrode in a three-electrode cell configuration and was coated with the produced slurry. The active material mass per unit area of the electrode is 0.95 mg. The counter and reference electrodes were a platinum wire and an Ag/AgCl electrode, respectively.

4 Results & Discussion

4.1 X-Ray Diffraction Study

Fig. 2a represents the XRD intensity patterns for GO, MoS_2, and the MoS_2/GO nanocomposite material with the diffraction peaks at 11.70° corresponding to the crystalline plane (001) for GO, whereas 14.5°, 33°, 39.30° and 58.50° correspond to (0 0 2), (1 0 0), (1 0 3) and (1 1 0) crystalline planes of MoS_2 [10]. When GO is added, the intensity peaks of MoS_2 nanoparticles decrease. As a result, adding GO slows down the phase transition and stops the crystallite from growing. MoS_2/GO nanocomposites in Fig. 2a represents the new peaks observed at $2\theta = 11.6^\circ$, 14.4°, 32.5°, 38.50°, and 57.90° that are indexed as (0 0 1), (0 0 2), (1 0 0), (1 0 3), and (1 1 0) [MoS_2 (0 0 2), (1 0 0), (1 0 3) and (1 1 0)] crystal planes are matching with the standard data (JCPDS Card No. 37-1492) [12]. The purity of the produced MoS_2/GO nanocomposites is confirmed by the absence of any additional impurity peaks from a phase.

4.2 Raman Spectroscopic Analysis of MoS_2/GO Nanocomposite

Raman spectroscopy was employed to elucidate the vibrational characteristics and structural integrity of the synthesized MoS_2/GO nanocomposite. The recorded Raman spectrum (Fig. 2b) exhibited distinct peaks at 277, 330, and 372 cm^{-1}, characteristic of MoS_2 [13]. The peaks at 277 and 372 cm^{-1} correspond with the $E^1{}_{2g}$ (in-plane vibration of Mo and S atoms) and A_{1g} (out-of-plane vibration of S atoms) modes, respectively. These modes confirm the presence of few-layered MoS_2, indicated by the frequency difference between the $E_{2g}{}^1$ and A_{1g} modes. In our study, the observed peaks at 277 and 372 cm^{-1} are indeed shifted compared to the ideal values. This shift can be attributed to several factors, including strong interaction between MoS_2 and GO in the nanocomposite, possible structural disorder, reduced layer thickness, strain effects, and defect-induced phonon softening. Such shifts in Raman modes have been reported in the literature for MoS_2-based composites and defect-engineered systems [14,15]. In addition, the peak observed at 330 cm^{-1} may be attributed to second-order Raman scattering or defect-induced vibrational modes, as reported in doped or composite MoS_2 systems, indicating a degree of structural distortion due to the incorporation of graphene oxide. Higher wavenumber features at 657, 816, and 991 cm^{-1} are assigned to vibrational modes involving oxygenated functional groups and possible Mo–O or S–O bonding [16], which may arise from surface oxidation or interfacial interaction between MoS_2 and GO. These bands suggest a strong chemical interaction at the MoS_2/GO interface, possibly facilitating charge transfer processes in photocatalytic or electrochemical applications. The broad bands at 1312 cm^{-1} and 1595 cm^{-1} represent the D band and the G band, respectively, and are indicative of the graphene oxide (GO) component [17]. The D band arises from defect-activated breathing modes of sp^2 carbon rings, which become Raman-active in the presence of structural disorder or functionalization, whereas the G band is attributed to the E_{2g} phonon of sp^2 carbon domains. The intensity ratio (I_D/I_G = 0.82) provides insight into the level of disorder and reduction of GO in the nanocomposite [18]. The observed spectral features confirm the successful integration of GO with MoS_2 and suggest a synergistic interaction that could enhance the composite's functional properties.

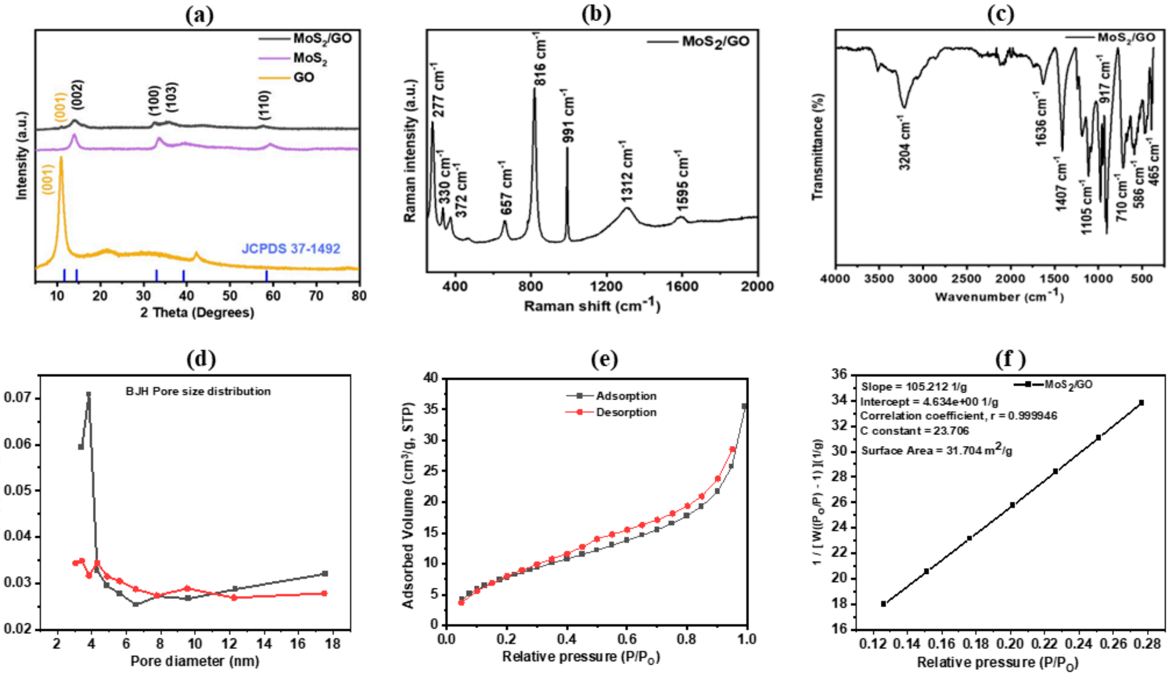

Figure 2: XRD Intensity patterns correspond to (**a**) GO, MoS_2, and the MoS_2/GO nanocomposite. (**b**) Raman spectra of MoS_2/GO nanocomposite. (**c**) FTIR spectra of MoS_2/GO nanocomposite. Nitrogen adsorption–desorption isotherm and corresponding BET analysis of the MoS_2/GO nanocomposite. (**d**) BJH pore size distribution curves of the MoS_2/GO nanocomposite derived from adsorption and desorption branches, showing a dominant mesoporous structure with a narrow pore size distribution centered around ~4 nm, indicative of enhanced electrolyte accessibility and efficient ion transport pathways. (**e**) N_2 adsorption–desorption isotherm showing a typical Type IV profile with a distinct H3-type hysteresis loop, indicating the presence of mesoporous structure with slit-shaped pores. (**f**) Brunauer–Emmett–Teller (BET) plot in the relative pressure (P/P_0) range of 0.12–0.28, exhibiting excellent linearity for surface area determination.

4.3 Fourier Transform Infrared Spectroscopy Analysis (FTIR) of MoS_2/GO Nanocomposite

The FTIR spectrum of the MoS_2/GO nanocomposite Fig. 2c displays characteristic peaks, suggesting the successful incorporation of both MoS_2 and graphene oxide. The broad spectral absorption around 3204 cm^{-1} is due to the O–H stretching vibration of hydroxyl groups and adsorbed water molecules on the GO surface [19]. The bending mode of adsorbed water (H–O–H) is represented by the band at 1636 cm^{-1}. and may also include contributions from aromatic C=C stretching within the GO sheets. A peak observed at 1407 cm^{-1} is associated with C–OH or C–C vibrational stretching modes, while the peak at 1105 cm^{-1} can be ascribed to C–O–C epoxy group vibrations, confirming the presence of oxygen-rich functional groups on GO [20]. Notably, the band at 917 cm^{-1} may be attributed to Mo=O and S–O stretching vibrations, indicating partial oxidation at MoS_2 edges or surface defects [17]. Distinct absorption bands at 710, 586, and 465 cm^{-1} are characteristic of Mo–S bond vibrations, corresponding to out-of-plane and in-plane modes as well as lattice vibrations of the hexagonal MoS_2 phase, respectively. These findings indicate that the MoS_2/GO composite was successfully synthesized, with the structural features of both components preserved.

4.4 Brunauer–Emmett–Teller (BET) Analysis

To corroborate the SEM observations, nitrogen adsorption–desorption analysis was performed to evaluate the surface area and porosity of the MoS_2/GO nanocomposite. As shown in Fig. 2e, the isotherm exhibits a typical Type IV profile with a pronounced hysteresis loop in the relative pressure (P/P_0) range of 0.4–1.0, confirming the presence of a mesoporous structure. The hysteresis loop is classified as H3-type, indicating slit-shaped pores formed due to the stacking and aggregation of layered MoS_2 nanosheets in conjunction with graphene oxide sheets. This observation is consistent with the SEM results, which show that incorporating GO prevents restacking and promotes the formation of a more open and accessible porous network. The Brunauer–Emmett–Teller (BET) surface area was calculated from the linear region of the isotherm (P/P_0 = 0.12–0.28), as shown in Fig. 2f, yielding an excellent linear fit ($R \approx 0.9999$), which confirms the validity of the BET model. The specific surface area was approximately 31.7 $m^2\ g^{-1}$, indicating moderate surface development. The BET constant ($C \approx 23.7$) suggests moderate adsorbate–adsorbent interactions, characteristic of physisorption.

Furthermore, the pore-size distribution profile obtained using the Barrett–Joyner–Halenda (BJH) method indicates that the nanocomposite predominantly consists of mesopores in the 2–50 nm range, with a relatively narrow distribution. The presence of these mesopores is crucial, as they facilitate efficient electrolyte diffusion and ion transport within the electrode matrix. The incorporation of GO sheets plays a key role in tailoring this porous architecture by preventing the dense stacking of MoS_2 layers, thereby enhancing pore accessibility and creating interconnected transport pathways. The pore size distribution obtained from the BJH method (Fig. 2d) reveals that the MoS_2/GO nanocomposite predominantly exhibits mesopores centered at ~3–10 nm, with a prominent peak near ~4 nm. The relatively narrow distribution indicates a uniform porous architecture, which can be attributed to the effective prevention of MoS_2 restacking by the incorporation of graphene oxide sheets. The desorption branch shows a sharper, more defined peak than the adsorption branch, confirming the reliability of the pore structure analysis. Such mesoporous characteristics are highly beneficial for electrochemical applications [21], as they facilitate rapid electrolyte diffusion and provide efficient ion transport pathways [22,23]. The presence of interconnected mesopores further enhances electrolyte accessibility, thereby improving the electrode material's overall electrochemical performance [24]. Overall, the combined BET and BJH analyses confirm that the MoS_2/GO nanocomposite possesses a well-defined mesoporous structure with improved electrolyte accessibility, which is expected to significantly enhance its electrochemical performance in energy storage applications.

4.5 Morphological & Elemental Composition Characterization

Fig. 3 presents the scanning electron microscopy (SEM) images and elemental mapping results of GO, MoS_2, and the MoS_2/GO nanocomposite. The SEM image of GO (Fig. 3a) shows a characteristic wrinkled and sheet-like morphology with thin, layered structures. These folded and crumpled sheets exhibit the typical exfoliated graphene oxide architecture, providing a high surface area and abundant active sites that are beneficial for anchoring nanomaterials. The SEM micrograph of MoS_2 (Fig. 3b) reveals a rod-like or stacked nanostructured morphology, with particles densely packed and irregularly oriented. Such morphology is commonly associated with layered MoS_2 structures formed during synthesis, which enhance catalytic and electrochemical activity due to their high edge exposure. The SEM image of the MoS_2/GO composite (Fig. 3c) clearly demonstrates the successful integration of MoS_2 nanostructures onto the GO sheets. The MoS_2 particles are uniformly distributed across the graphene oxide surface, forming a hybrid layered structure. The GO sheets act as a conductive support matrix, preventing agglomeration of MoS_2 particles while enhancing surface area and charge-transport pathways. Elemental composition and spatial distribution were further confirmed using energy-dispersive X-ray spectroscopy (EDAX) mapping. The EDAX scanned image (Fig. 3d) illustrates the overall morphology of the analyzed region. Elemental mapping of molybdenum (Mo Lα1) in Fig. 3e shows a homogeneous distribution of Mo throughout the composite structure, indicating successful incorporation of MoS_2 within the GO matrix. Similarly, the sulfur mapping (S Kα1) shown in Fig. 3f confirms the presence and uniform dispersion of sulfur elements, which correspond to the MoS_2 phase. The uniform spatial distribution of Mo and S elements strongly verifies the formation of the MoS_2/GO composite without significant phase segregation. This homogeneous dispersion is expected to enhance interfacial interactions between MoS_2 and GO, thereby improving electrical conductivity, active surface area, and overall performance of the composite in electrochemical and catalytic applications.

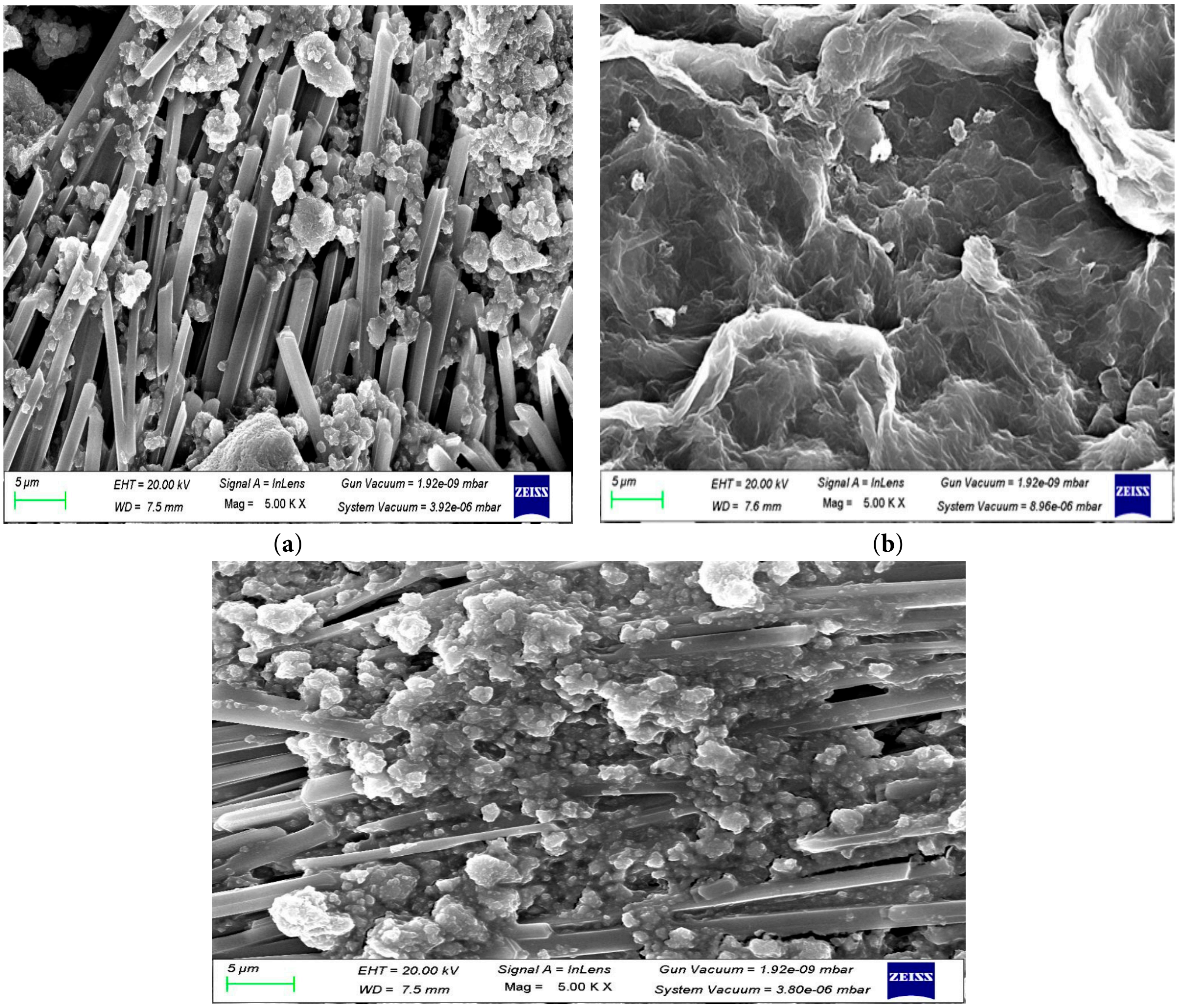

(**a**) (**b**)

(**c**)

Figure 3: *Cont.*

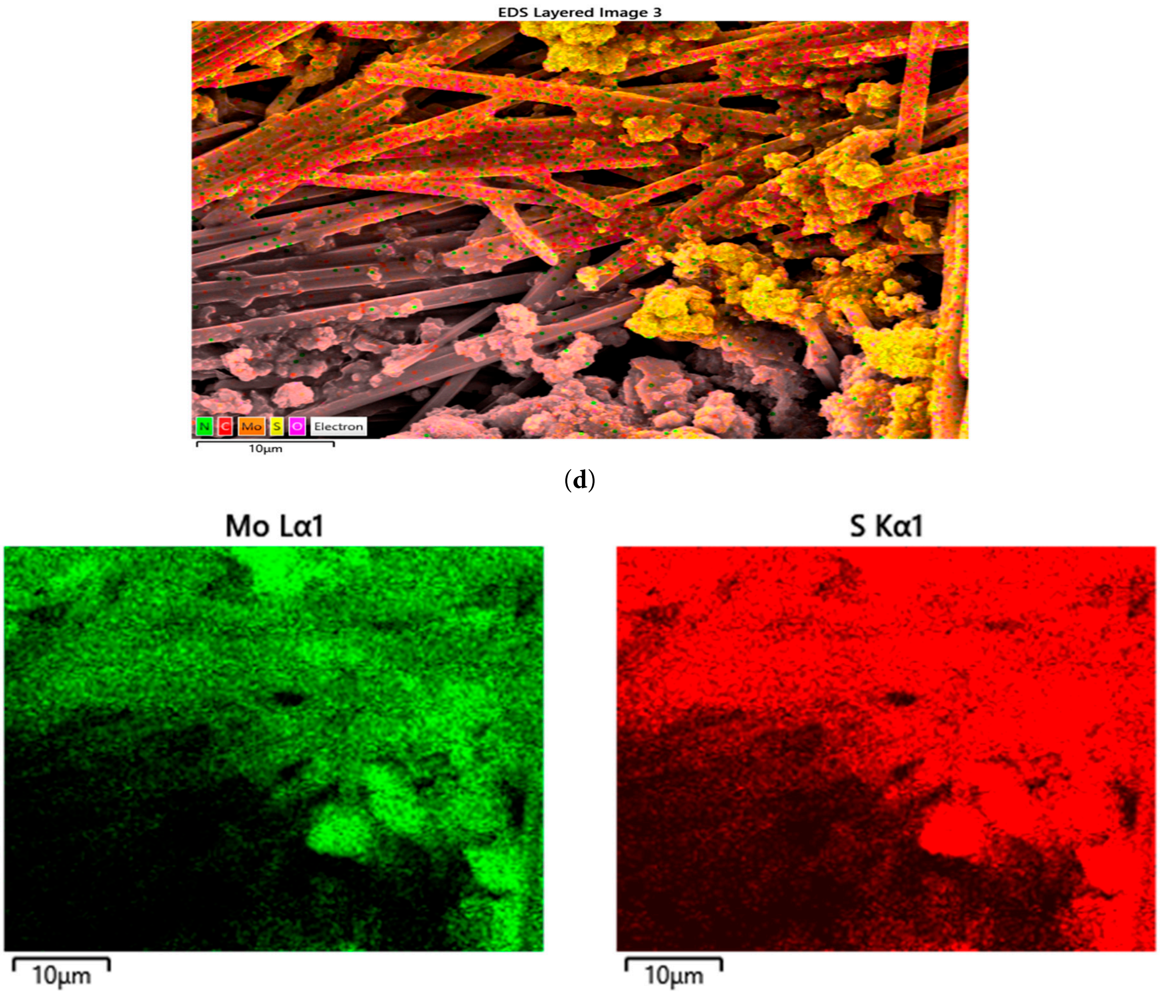

(**d**)

(**e**) (**f**)

Figure 3: Scanning electron microscope images of (**a**) GO, (**b**) MoS_2, (**c**) MoS_2/GO, (**d**) EDAX scanned image of MoS_2/GO, (**e**) Mo Lα1, (**f**) S Kα1 mapped image.

4.6 Electrochemical Analysis

For electrochemical testing of pristine MoS_2 and MoS_2/GO nanocomposites, the electrolyte used was 2 M KOH. Cyclic voltammetry was employed to assess the electrode material's electrochemical behavior, which is important for understanding the energy storage mechanism; specific capacitance was determined from cyclic voltammetry curves using the formula [25].

$$\mathrm{C} = \frac{\int idV}{2mv\Delta V} \tag{1}$$

where m represents the working electrode material mass in grams (g); v denotes the scan rate measured in millivolts per second (mV/s); and ΔV corresponds to the operating voltage range in volts (V).

The charge-discharge kinetics were analyzed using chronopotentiometry. From the CP curves, the formula given by expression (2) is used to determine the electrode material's specific capacitance [26].

$$\mathrm{C} = \frac{i\Delta t}{m\Delta V} \tag{2}$$

In this equation, i denotes the current density (A), m represents the mass of the active material (g), ΔV corresponds to the voltage window (V), and Δt is the discharge time (s).

The Electrochemical analysis of pristine MoS_2 is shown in Fig. 4a–d. The Cyclic voltammetry (CV) curves in Fig. 4a illustrate the relationship between current and potential at scan rates ranging from 5 to 100 mV s^{-1}. As the scan rate increases, the area enclosed by the cyclic voltammetry (CV) curve also expands, reflecting superior capacitive behavior. The quasi-rectangular shape of the CV curves indicates a hybrid of pseudocapacitive and electric double-layer capacitance (EDLC) characteristics, typical of MoS_2-based electrodes. The Chronopotentiometric curves (CP) shown in Fig. 4b illustrate the voltage-time variation over a range of current densities from 0.5 to 2.5 A g^{-1}. The deviation from linearity in the curves suggests the presence of faradaic reactions, further confirming the pseudocapacitive contribution. Discharge time decreases with rising current density, suggesting a drop in specific capacitance.

The graph shown in Fig. 4c demonstrates the dependence of specific capacitance on scan rate. A notable decline in specific capacitance is observed as the scan rate increases, indicating that ion diffusion is hindered at higher scan rates, limiting electrode surface utilization. The graph depicted in Fig. 4d illustrates how specific capacitance varies with current density.

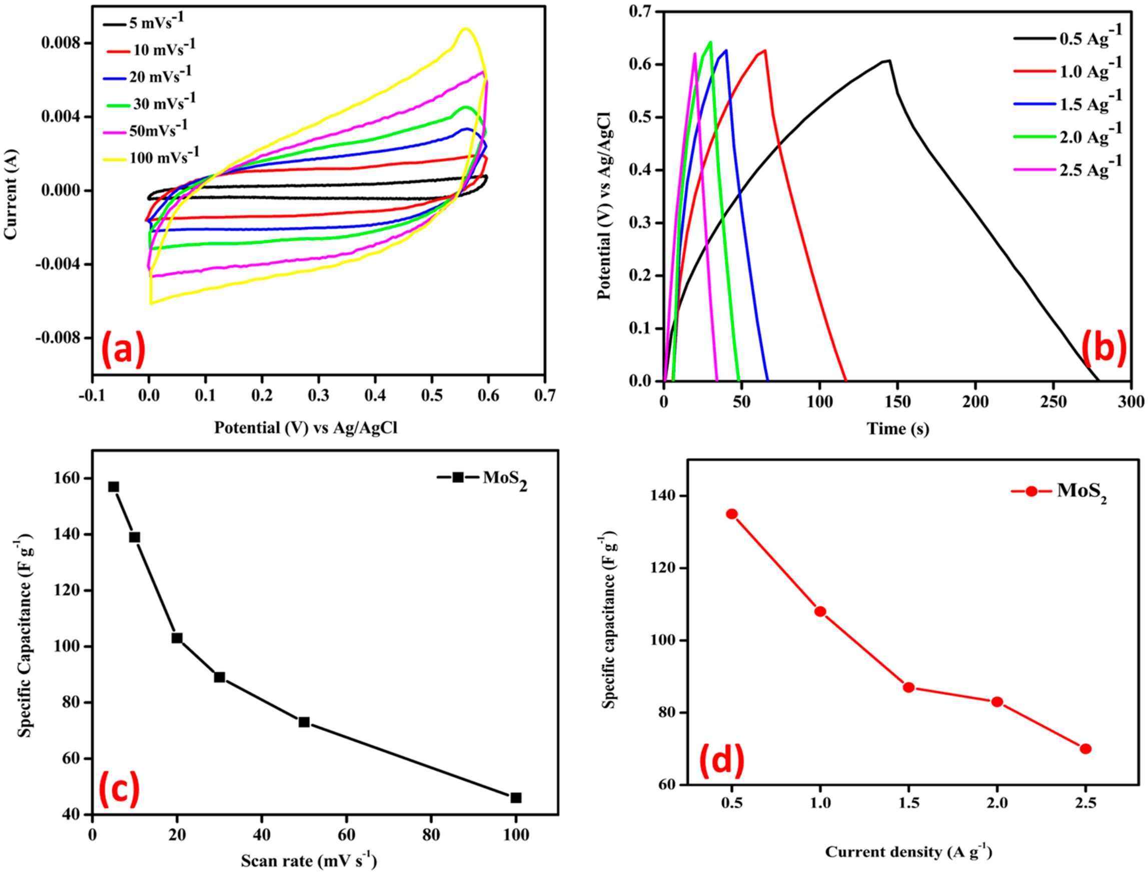

Figure 4: (**a**) Cyclic Voltammetric curve of MoS_2, (**b**) Charging-discharging curve of MoS_2, (**c**) Calculated specific capacitance under different scan rates, (**d**) Calculated specific capacitance under different current densities.

A steady decrease in specific capacitance is evident as current density increases, due to reduced ion diffusion and limited access to the active surface area. This behavior reflects typical characteristics of MoS_2 electrodes, which exhibit good rate capability but with a gradual decline in capacitance at higher current loads. Overall, the electrochemical analysis suggests that MoS_2 exhibits a combination of EDLC and pseudocapacitive behavior, making it a good choice for energy storage applications [27].

The cyclic voltammetry (CV) plot in Fig. 5a illustrates the electrochemical behavior of the MoS_2/GO composite over a steady potential range of −0.1–0.7 V, recorded at scan rates varying from 5 mV/s to 100 mV/s. The quasi-rectangular shape of the CV curves indicates pseudocapacitive behavior arising from faradaic redox processes and the electric double-layer capacitance at the active sites of MoS_2 and the oxygen functional groups in GO [28]. At lower scan rates, the curves exhibit a well-defined quasi-rectangular profile with clear faradaic contributions. This suggests sufficient time for ion diffusion and redox reactions at the electrode interface [29]. As the scan rate increases, the current response grows proportionally, indicating enhanced charge storage performance. However, at higher scan rates, the curves deviate slightly from ideal rectangularity. This deviation is due to kinetic limitations, in which ion diffusion within the electrode material becomes less effective, and the redox reactions become rate-limited. The increasing peak currents of the anode and cathode with scan rate suggest a good reversibility of the redox reactions. Additionally, the broad peak separation at higher scan rates indicates that charge-transfer kinetics are slightly hindered by increased resistance or limited ion mobility [30]. This is characteristic of systems where both diffusion-controlled and surface-controlled processes contribute to the overall capacitance [31]. Fig. 5b represents CP curves of the MoS_2/GO composite measured at current density values varying from 0.5 A/g to 2.5 A/g, demonstrating excellent electrochemical performance. The CP curves exhibit nearly linear, symmetrical charge-discharge characteristics, confirming high electrochemical reversibility and capacitive behavior.

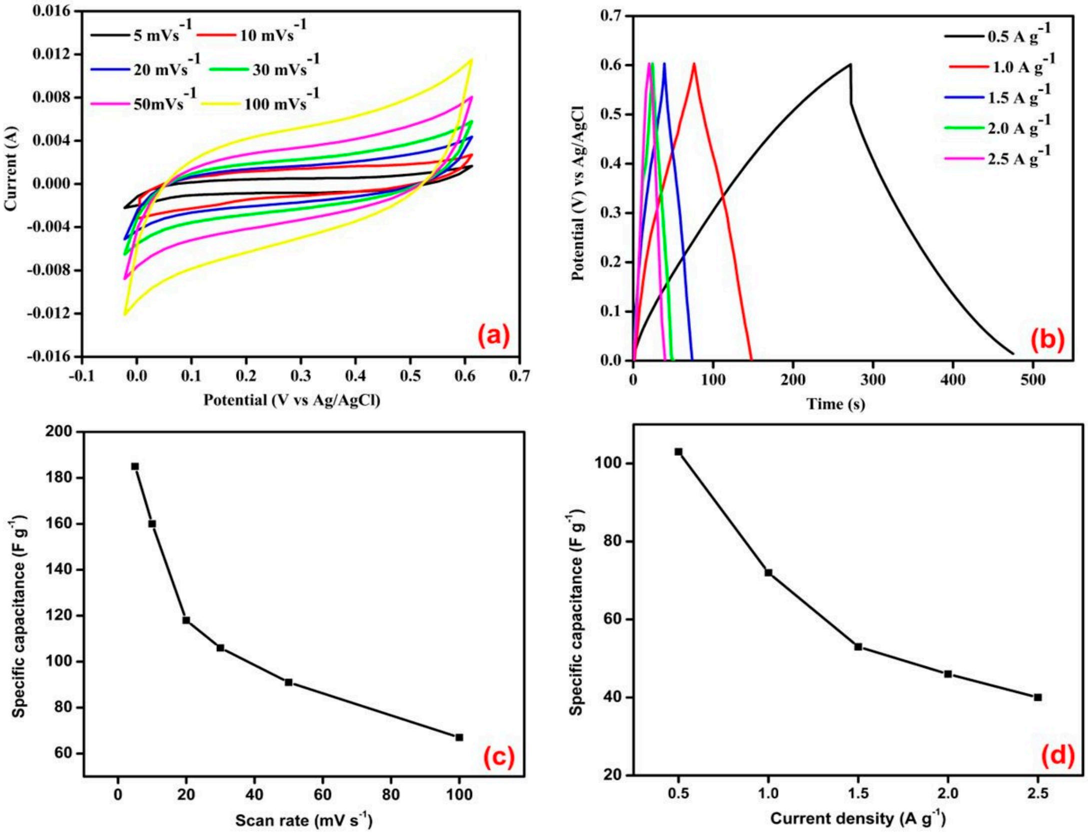

Figure 5: (**a**) CV curve of MoS_2/GO, (**b**) CP curve of MoS_2/GO, (**c**) Calculated specific capacitance under different scan rates, (**d**) Calculated specific capacitance under different current densities.

At lower current densities, such as 0.5 A/g, the longer discharge times reflect higher specific capacitance, as ions have adequate time to access the electrode's reactive sites. Conversely, at higher current densities, such as 2.5 A/g, discharge times decrease due to the rapid charge/discharge process, which hinders ion diffusion within the material. The absence of significant IR drops in the curves highlights the low internal resistance and good composite's electrical conductivity. The linear profiles suggest that the energy storage mechanism is dominated by pseudocapacitive behavior, involving reversible faradaic reactions and electric double-layer capacitance. The combination of MoS_2, which provides redox-active sites, and graphene oxide GO, which enhances conductivity and ion transport, synergistically adds to the high specific capacitance of the material, good rate capability, and suitability for supercapacitor applications [32]. The specific capacitance at different scan rates and current densities is shown in Fig. 5c,d. Fig. 6a depicts the electrochemical impedance spectra, which illustrate the impedance behavior of the MoS_2/GO electrode before and after the cycling stability test. The graph consists of two distinct regions: a semicircular high-frequency region and a linear low-frequency region. The semicircle in the Nyquist plot observed at high frequencies corresponds to the charge transfer resistance (R_{ct}) at the electrode/electrolyte interface, while the straight line at low frequencies corresponds to the Warburg impedance, which indicates ion diffusion within the electrode material [33]. Before cycling, the electrode shows a smaller semicircle, indicating reduced charge-transfer resistance (Rct) and improved electrical conductivity. After cycling, the semicircle becomes slightly larger, suggesting an increase in charge transfer resistance due to electrode degradation or reduced conductivity [34]. The straight line in the low-frequency region, which is closer to 45° before cycling, reflects efficient ion diffusion within the electrode. After cycling, the slope of this line decreases, indicating a slight decline in ion diffusion caused by structural changes or the loss of active sites. The EIS results confirm that the MoS_2/GO electrode maintains good conductivity and ion diffusion properties even after cycling [35]. The slight increase in impedance underscores the composite material's stability and durability, making it a potential electrode for stable, long-term supercapacitor performance.

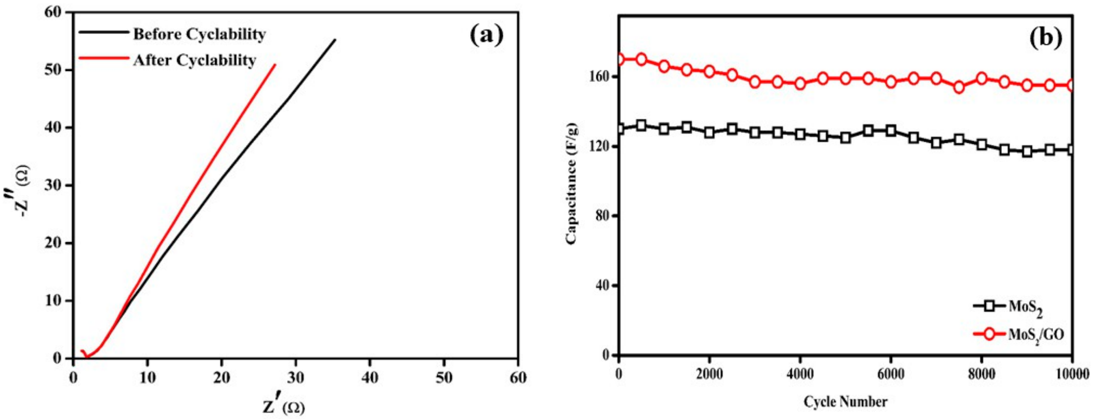

Figure 6: (**a**) The Nyquist plot of MoS_2/GO electrode material; (**b**) Cyclic stability of MoS_2 and MoS_2/GO up to 10,000 cycles.

The graph as depicted in Fig. 6b illustrates the cycling stability of MoS_2 and MoS_2/GO, showing their specific capacitance (F/g) over 10,000 charge-discharge cycles. The capacitance of MoS_2 initially decreases and then gradually declines, indicating structural degradation, increased charge-transfer resistance, and loss of active material over time [36]. In contrast, MoS_2/GO maintains a consistently higher capacitance with minimal fading, demonstrating superior electrochemical stability than MoS_2. This enhancement is attributed to the synergistic effect of GO, which provides a highly conductive network, reduces internal resistance, and prevents aggregation and restacking of MoS_2 nanosheets, thereby maintaining an active surface area for ion diffusion. Additionally, the oxygen functional groups in GO improve electrolyte wettability, facilitating efficient electrochemical reactions. The high capacitance retention of MoS_2/GO indicates robust structural integrity and resistance to electrode pulverization, making it a promising material for next-generation energy storage devices such as lithium-ion batteries and supercapacitors. Table 1 summarizes the supercapacitor performance of various MoS_2-based electrode materials reported in the literature [37–45].

Table 1: Supercapacitor performance of various MoS_2 electrode materials.

S. No.	Electrode Material	Electrolyte	Specific Capacitance (F/g)	Measuring Parameter	Ref.
1	N-doped Graphene/MoS_2	6 M KOH	227	1 A/g	[37]
2	MoS_2 nanosheets	1 M Na_2SO_4	129.2	1 A/g	[38]
3	Graphene/MoS_2	PVA/Na_2SO_4	202	10 mV/s	[39]
4	MoS_2 nanoporous films	1 M LiOH	14.5	1 A/g	[40]
5	MoS_2 nanodots	6 M KOH	122	1 A/g	[41]
6	O- and N-doped MoS_2 microspheres	6 M KOH electrolyte	84.82	1 A/g	[42]
7	MoS_2-Co–C	6 M KOH	71	0.2 A/g	[43]
8	MoS_2/reduced graphene oxide (MoS_2/rGO)	1 M $HClO_4$	265	10 mV/s	[44]
9	MoS_2@FeS_2	6 M KOH	186	1 A/g	[45]
10	MoS_2/GO	2 M KOH	185	5 mV/s	This Work

4.7 Electrochemical Surface Area (ECSA) Determination

The electrochemical surface area (ECSA) was evaluated by analyzing the double-layer capacitance (Cdl) derived from cyclic voltammetry (CV) measurements performed at varying scan rates (20–100 mV s^{-1}) in a non-faradaic potential window (~0.30 V). The capacitive current density ($\Delta j = |ja - jc|$) was calculated by taking the difference between anodic and cathodic current densities at the selected potential. A linear dependence of Δj on scan rate (ν) was observed, consistent with ideal capacitive behavior. The relationship follows:

$$\Delta j = 2Cdl\nu \tag{3}$$

The slope obtained from the linear fit corresponds to twice the double-layer capacitance. The calculated Cdl value is ~62 mF cm^{-2}, indicating a high density of electrochemically active sites.

In Fig. 7, the plot shows the variation of current density difference (Δj) as a function of scan rate (20–100 mV s^{-1}) in the non-faradaic region. The linear fit ($R^2 = 0.927$) indicates predominant double-layer capacitive behavior. The goodness of fit ($R^2 = 0.927$) confirms a reasonably linear capacitive response, although slight deviations at lower scan rates suggest minor non-ideal contributions.

The slope was used to calculate the double-layer capacitance (Cdl), which was then used to estimate the ECSA.

The ECSA was estimated using:

$$ECSA = \frac{Cdl}{Cs} \tag{4}$$

where Cs (0.04 mF cm^{-2}) represents the specific capacitance of a smooth surface in alkaline electrolyte. The calculated ECSA is ~1550 cm^2, indicating a significantly higher active surface area due to the material's porous, nanostructured morphology.

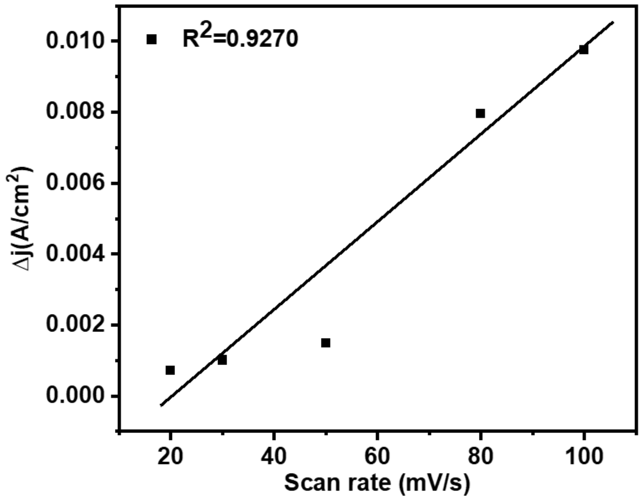

Figure 7: Determination of electrochemical surface area (ECSA) using capacitive current analysis.

4.8 DFT Calculations

Structural and Computational Details

Both molybdenum disulfide (MoS_2) and GO exhibit a hexagonal structure with the $P6_3/mmc$ space group (No. 194), as shown in Fig. 8a,b. The electronic structural properties and density of states of GO and MoS_2 were investigated using first-principles density functional theory (DFT) calculations with plane-wave basis sets and ultrasoft pseudopotentials, implemented in the Quantum ESPRESSO package [46].

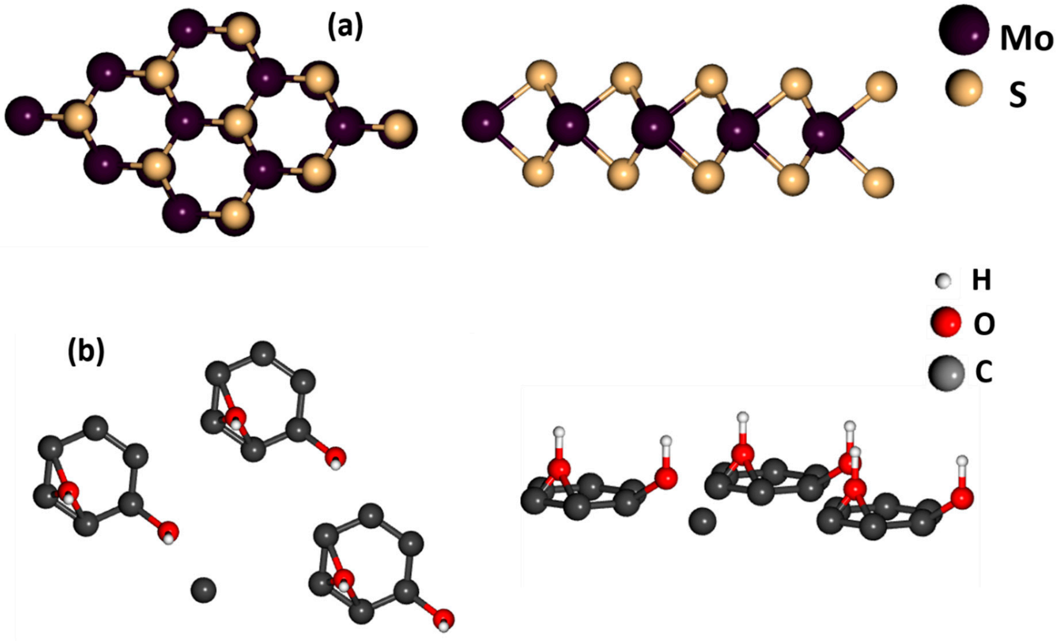

Figure 8: (**a**) MoS_2 in both top and side views; (**b**) GO in both top and tilted views.

The exchange–correlation energy was described using the generalized gradient approximation (GGA) with the Perdew–Burke–Ernzerhof (PBE) functional [47]. While the GGA-PBE functional is known to slightly underestimate the absolute band gap compared to hybrid functionals, it reliably captures the key qualitative features and trends in the electronic density of states discussed in this work. Plane-wave basis sets with a kinetic energy cutoff of 65 Ry and a charge-density cutoff of 300 Ry were employed. The total energy convergence criterion was set to be better than 10^{-7} eV. A Monkhorst–Pack k-point mesh of 12 × 12 × 12 was used for structural optimization and electronic structure calculations. The calculations in this work were performed using a 3 × 3 × 1 supercell with periodic boundary conditions and a vacuum spacing of ~15–20 Å along the out-of-plane direction to avoid interlayer interactions. For the density of states (DOS) and partial density of states (PDOS) calculations, a denser 31 × 31 × 31 k-point grid was applied. During cell relaxation, the pressure convergence threshold was fixed at 10^{-4} kbar, while the force convergence criterion for ionic relaxation was set to 10^{-4} Ry/Bohr. An analysis of the electronic band structures and density of states (DOS) of MoS_2 and GO was carried out, and the results are shown in Fig. 9a–d. By determining each system's minimum energy, lattice relaxation was achieved, allowing the lattice parameters to be optimized for each system [48]. The optimal lattice values for the MoS_2 and GO compounds are 3.19 Å and 2.49 Å, respectively. The atoms that contribute to the formation of the band structure are shown by comparing the density of states (DOS) plots for GO and MoS_2, which is shown in Fig. 10. At the same time, according to Marcus formulation and Gerischer's formulation, electrons are transferred from the metal/semiconductor electrodes occupied electronic states. The nanoscale electrode DOS (ρ(E)) then determines the electron-transfer kinetic rate (ket). It can be advantageous to investigate the quantum electronic states, as characterized by the density of states (DOS), in nanostructured electrodes and to understand their dependence on the individual materials in nanocomposites, given that nanomaterial composites operate in the quantum world. In the quantum-mechanical case, capacitance is mostly determined by the density-of-states distributions of the electrode materials. Quantum capacitance (Cq) is a phenomenon caused by the charging up of quantum states at the atomic and molecular levels. Cq has a major influence on nanoscale materials, whereas its effect is minimal in bulk materials. It is anticipated that selecting an appropriate nanomaterial with a high Cq is essential for achieving the best possible electrochemical device performance, as the material DOS is closely correlated with Cq ($Cq \propto \rho(E)$) near the Fermi energy (Ef) [49,50]. Increased availability of electronic states typically results in increased electrical conductivity, as shown in Fig. 10. A higher DOS may improve electrical conductivity by providing more electrons to participate in conduction [4]. In some reactions, particularly those that require electron-transfer mechanisms, the material may thus perform better. The density of states (DOS) near the Fermi level (Ef) for GO is noticeably higher than that of MoS_2, as illustrated in Fig. 10. According to earlier observations, electrons that are carried from the electrolyte to the electrode surface occupy energy levels that are near the Ef [4,51]. As a result, GO electrodes are more likely than MoS_2 to have a higher number of electrons occupying several energy levels. The greater DOS at Ef, which leads to faster electron-transfer kinetics at the interface, is also observed in electrochemical spectroscopy. In the present study, the GO shows better surface electrochemistry than MoS_2, indicating the great potential of these (and possibly the MoS_2/GO composite) for the development of electrochemical devices, including biosensors, batteries, supercapacitors, and electrochromic systems.

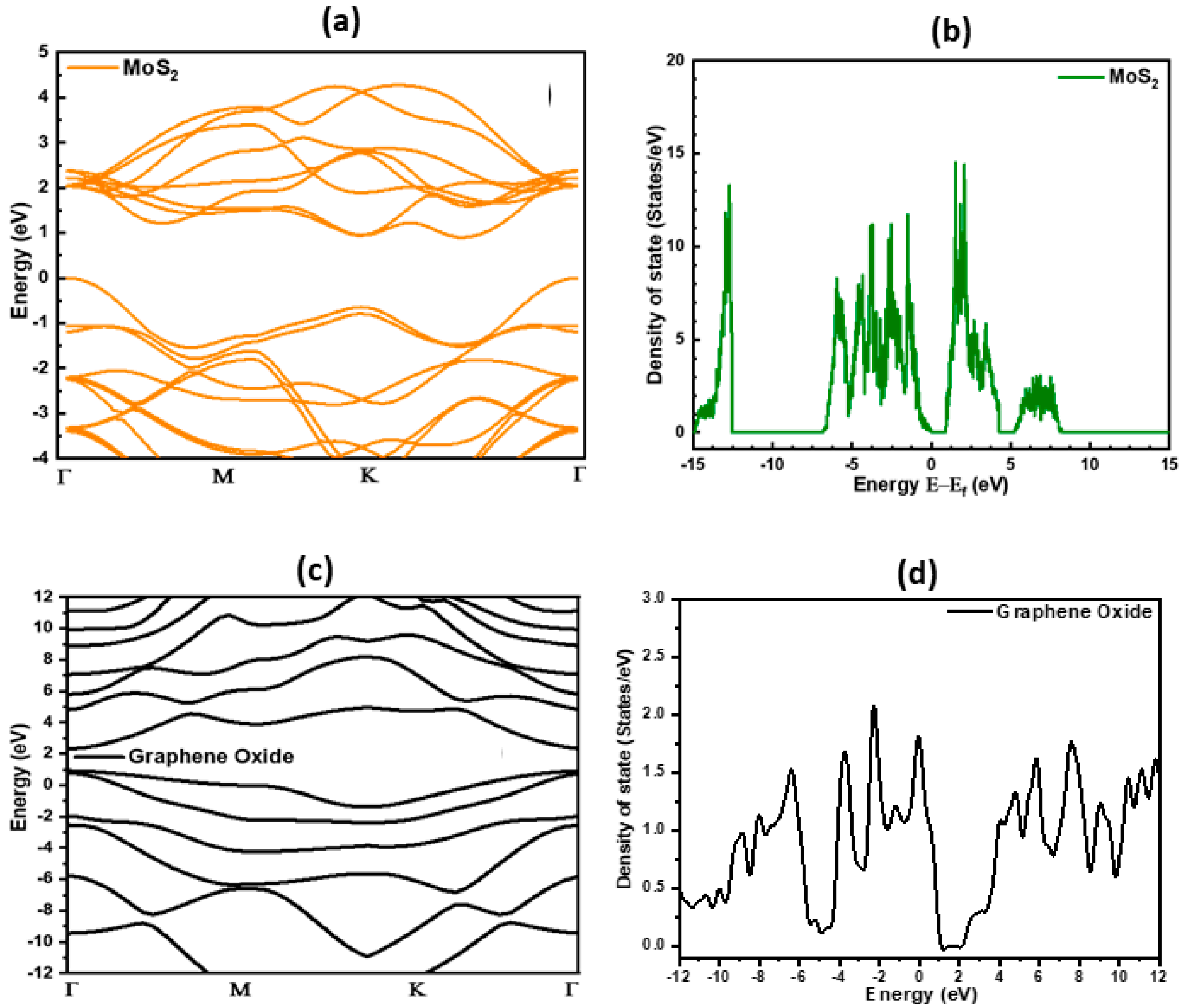

Figure 9: (**a**) Band structure of MoS$_2$; (**b**) density of state plots of MoS$_2$; (**c**) Band structure of graphene oxide GO and (**d**) density of state plots of GO graphene oxide.

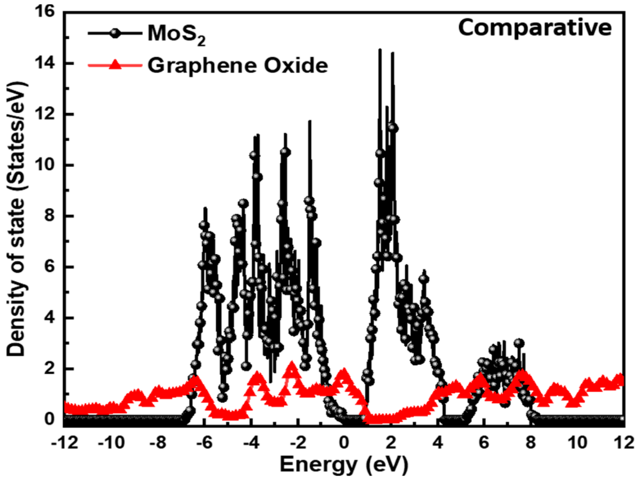

Figure 10: A comparison between the MoS$_2$ and GO Density of states.

5 Conclusions

In this work, we demonstrate that GO doping is an effective strategy for enhancing the electrochemical properties of MoS_2. GO/MoS_2 was characterized by XRD, which showed that upon GO addition, the intensity of the MoS_2 nanoparticle peaks decreased. SEM revealed MoS_2 rod-like morphology with a layered structure, and EDAX analyzed the elemental composition of Mo, S, O, and C. The density of states (DOS) analysis of isolated systems indicates that graphene oxide (GO) exhibits a higher DOS near the Fermi level than MoS_2, which may be beneficial for supercapacitor electrode applications, such as in MoS_2/GO nanocomposites. However, in the actual composite system, charge transfer and Fermi level alignment between MoS_2 and GO can influence the overall electronic structure. The DFT calculations also show that the 2D GO has a higher DOS near the Fermi level than MoS_2, indicating an enhanced quantum capacitance, which is advantageous for supercapacitor electrode materials such as MoS_2/GO nanocomposites. Electrochemical analyses using the MoS_2/GO nanocomposite showed an enhanced specific capacitance of 185 F g^{-1}. Higher DOS may improve electrical conductivity by providing more electrons to participate in conduction, as measured at a scan rate of 5 mV s^{-1}. By powering a real-world gadget, our work demonstrates practical utility and deepens our understanding of material modifications for energy applications.

Acknowledgement: We thank Dr. Mohammad Jane Alam, Department of Physics at AMU, Aligarh, for working as a research volunteer. The authors also acknowledge the High-Speed Computing (HPC) facility at IUAC in New Delhi and Galgotias University in Greater Noida, Uttar Pradesh.

Funding Statement: The authors received no specific funding for this study.

Author Contributions: The authors confirm contribution to the paper as follows: study conception and design: Mohsin Sayeed, O. P. Singh, Azam Raza; data collection: Mohammad Shariq, Navshad Alam; analysis and interpretation of results: Mohsin Sayeed, O. P. Singh, Vishal Singh Chandel, Azam Raza, Kamal Batcha Mohamed Ismail; draft manuscript preparation: Mohsin Sayeed, Azam Raza, Mayur Khan, Kamal Batcha Mohamed Ismail. All authors reviewed and approved the final version of the manuscript.

Availability of Data and Materials: Data and materials can be made available on request.

Ethics Approval: Not applicable.

Conflicts of Interest: The authors declare no conflicts of interest.

References

1. Becchetti L, Solferino N, Tessitore ME. The sustainable future is now: A dynamic model to advance investments in PV and energy storage. Renew Energy. 2026;260:125181. [CrossRef].
2. Gupta D, Chauhan V, Kumar R. A comprehensive review on synthesis and applications of molybdenum disulfide (MoS_2) material: Past and recent developments. Inorg Chem Commun. 2020;121:108200. [CrossRef].
3. Yilmazoğlu E, Karakuş S. Recent developments in nanostructured materials for supercapacitor electrodes. J Turk Chem Soc Sect A Chem. 2023;10(4):1107–22. [CrossRef].
4. Priyadharshini A, Vinodhini SP, Xavier JR. A comprehensive review of graphene-based nanocomposites for high-performance energy storage: Advances in design, electrochemical mechanisms, and future prospects. Ionics. 2026;32(3):2483–520. [CrossRef].
5. Sahoo PK, Kumar N, Jena A, Mishra S, Lee CP, Lee SY, et al. Recent progress in graphene and its derived hybrid materials for high-performance supercapacitor electrode applications. RSC Adv. 2024;14(2):1284–303. [CrossRef].
6. Ismail KBM, Arun Kumar M, Mahalingam S, Kim J, Atchudan R. Recent advances in molybdenum disulfide and its nanocomposites for energy applications: Challenges and development. Materials. 2023;16:4471. [CrossRef].

7. Han M, Mu Y, Guo J, Wei L, Zeng L, Zhao T. Monolayer MoS_2 fabricated by *in situ* construction of interlayer electrostatic repulsion enables ultrafast ion transport in lithium-ion batteries. Nanomicro Lett. 2023;15(1):80. [CrossRef].
8. Siao MD, Shen WC, Chen RS, Chang ZW, Shih MC, Chiu YP, et al. Two-dimensional electronic transport and surface electron accumulation in MoS_2. Nat Commun. 2018;9:1442. [CrossRef].
9. Li Y, Wang H, Xie L, Liang Y, Hong G, Dai H. MoS_2 nanoparticles grown on graphene: An advanced catalyst for the hydrogen evolution reaction. J Am Chem Soc. 2011;133(19):7296–9. [CrossRef].
10. Sayeed M, Maslamani N, Alhashem ZH, Al-Farhan AM, Sadaf S, Singh OP, et al. Spinel oxide–sulfide $MnCo_2O_4@MoS_2$ nanohybrids composite electrocatalyst for bifunctional water electrolysis. J Power Sources. 2026;673:239771. [CrossRef].
11. Hummers WS Jr, Offeman RE. Preparation of graphitic oxide. J Am Chem Soc. 1958;80(6):1339. [CrossRef].
12. Le Ngoc L, Pham Trung K, Tran Van K. Synthesis of MoS_2/graphene nanocomposite by facile ultrasonic-assisted hydrothermal method. Vietnam J Sci Technol. 2019;57(6):703–13. [CrossRef].
13. Sarma S, Mbule P, Ray SC. Layer-by-layer MoS_2: GO composite thin films for optoelectronics device applications. Appl Surf Sci. 2019;479:1118–23. [CrossRef].
14. Lee C, Yan H, Brus LE, Heinz TF, Hone J, Ryu S. Anomalous lattice vibrations of single- and few-layer MoS_2. ACS Nano. 2010;4(5):2695–700. [CrossRef].
15. Finardi AM, Fasolato C, Giugni A, Capeccia M, Cucini R, Cappelluti E, et al. Transient photodoping and phonon dynamics in bulk and monolayer MoS_2 by time resolved Raman scattering. npj 2D Mater Appl. 2025;9:79. [CrossRef].
16. Hingangavkar GM, Kadam SA, Ma YR, Bandgar SS, Mulik RN, Patil VB. MoS_2-GO hybrid sensor: A discerning approach for detecting harmful H_2S gas at room temperature. Chem Eng J. 2023;472:144789. [CrossRef].
17. Mao Z, Zhu H, Peng X, Chen J, Chen Q, Chen X, et al. *In situ* vertical alignment of 2D MoS_2 layers on GO film: Enhanced electrochemical properties for PD-L1 sensing. Microchim Acta. 2022;189(4):155. [CrossRef].
18. Kumar S, Sahoo PK, Satpati AK. Electrochemical and SECM investigation of MoS_2/GO and MoS_2/rGO nanocomposite materials for HER electrocatalysis. ACS Omega. 2017;2(11):7532–45. [CrossRef].
19. Rahaman S, Raza A, Lone AR, Muaz M, Zaidi SH, Adeeb MA, et al. Eco-friendly synthesis of an α-Fe_2O_3/rGO nanocomposite and its application in high-performance asymmetric supercapacitors. Phys Chem Chem Phys. 2024;26(22):16273–86. [CrossRef].
20. Dreyer DR, Park S, Bielawski CW, Ruoff RS. The chemistry of graphene oxide. Chem Soc Rev. 2010;39:228–40. [CrossRef].
21. Kim J, Youn S, Baek JY, Kim DH, Kim S, Lee W, et al. Modulation of conductivity and contact resistance of RuO_2 nanosheets via metal nano-particles surface decoration. Nanomaterials. 2021;11(9):2444. [CrossRef].
22. Jang JS, Lee SE, Choi SJ, Koo WT, Kim DH, Shin H, et al. Heterogeneous, porous 2D oxide sheets via rapid galvanic replacement: Toward superior HCHO sensing application. Adv Funct Mater. 2019;29(42):1903012. [CrossRef].
23. Jung SI, Nasir M, Park HJ. Ultrastable cycling in $Li_{1.5}Al_{0.5}Ge_{1.5}(PO_4)_3$-based solid electrolytes via Pt-engineered interfaces. ACS Appl Energy Mater. 2025;8(13):9302–10. [CrossRef].
24. Park JS, Nasir M, Kim D, Jeong HM, Park HJ. Engineering current collector with 2D TiO_2 nanosheets for stable lithium metal batteries. Batter Supercaps. 2025;8(8):e202400741. [CrossRef].
25. Ismail MM, Vigneshwaran J, Arunbalaji S, Mani D, Arivanandhan M, Jose SP, et al. Antimonene nanosheets with enhanced electrochemical performance for energy storage applications. Dalton Trans. 2020;49(39):13717–25. [CrossRef].
26. Ismail KBM, Kumar MA, Jayavel R, Arivanandhan M, Ismail MAM, Mahalingam S, et al. Optimized energy storage with hydrothermally synthesized metal sulfide nanocomposite electrodes. Colloids Surf A Physicochem Eng Asp. 2024;702:135138. [CrossRef].
27. Castro-Gutiérrez J, Celzard A, Fierro V. Energy storage in supercapacitors: Focus on tannin-derived carbon electrodes. Front Mater. 2020;7:217. [CrossRef].
28. Thangappan R, Kalaiselvam S, Elayaperumal A, Jayavel R, Arivanandhan M, Karthikeyan R, et al. Graphene decorated with MoS_2 nanosheets: A synergetic energy storage composite electrode for supercapacitor applications. Dalton Trans. 2016;45(6):2637–46. [CrossRef].
29. Ramalingam RJ, Konikkara N, Al-Lohedan H, Al-dhayan DM, Kennedy LJ, Khadheer Basha SK, et al. Synthesis of MoS_2 nanoparticle deposited graphene/mesoporous MnO_x nanocomposite for high performance super capacitor application. Int J Hydrogen Energy. 2018;43(36):17121–31. [CrossRef].

30. Patil UM, Nam MS, Kang S, Sohn JS, Sim HB, Kang S, et al. Fabrication of ultra-high energy and power asymmetric supercapacitors based on hybrid 2D MoS_2/graphene oxide composite electrodes: A binder-free approach. RSC Adv. 2016;6(49):43261–71. [CrossRef].
31. Yin X, Teng A, Zeng Z, Meng H, Wu W. Facile and scalable preparation of 2D-MoS_2/graphene oxide composite for supercapacitor. Ionics. 2022;28(11):5223–32. [CrossRef].
32. Hacinecipoglu AV, Gencten M. Efficient electrochemical synthesis of 2H-MoS_2/S-doped graphene oxide composites for binder-free high-performance supercapacitor electrodes. FlatChem. 2025;49:100800. [CrossRef].
33. Guo XL, Zhang YF, Li SY, Li Q, Hao Q, Ran XY, et al. Molybdenum disulfide carbon composite material using hydrothermal method as electrode material for supercapacitors. Chalcogenide Lett. 2025;22(4):313–30. [CrossRef].
34. Pan H, Lin J, Han X, Li Y, Meng X, Luo R, et al. Assembly of 1T'-MoS_2 based fibers for flexible energy storage. Nanoscale. 2020;12(11):6562–70. [CrossRef].
35. Xu G, Chen S, Liu Y, Fan W. A novel binder-free electrode of graphene film upon intercalation of hollow MoS_2 spheres for enhanced supercapacitor performance. Funct Mater Lett. 2018;11(4):1850074. [CrossRef].
36. Islam MR, Afroj S, Karim N. Scalable production of 2D material heterostructure textiles for high-performance wearable supercapacitors. ACS Nano. 2023;17(18):18481–93. [CrossRef].
37. Xie B, Chen Y, Yu M, Sun T, Lu L, Xie T, et al. Hydrothermal synthesis of layered molybdenum sulfide/N-doped graphene hybrid with enhanced supercapacitor performance. Carbon. 2016;99:35–42. [CrossRef].
38. Huang KJ, Zhang JZ, Shi GW, Liu YM. Hydrothermal synthesis of molybdenum disulfide nanosheets as supercapacitors electrode material. Electrochim Acta. 2014;132:397–403. [CrossRef].
39. Pilathottathil S, Kavil J, Thayyil MS. MoS_2 incorporated carbon allotropes (activated carbon, graphene, MWCNT) as electrodes in symmetric supercapacitors. J Indian Chem Soc. 2021;98(10):100169. [CrossRef].
40. Yang Y, Fei H, Ruan G, Xiang C, Tour JM. Edge-oriented MoS_2 nanoporous films as flexible electrodes for hydrogen evolution reactions and supercapacitor devices. Adv Mater. 2014;26(48):8163–8. [CrossRef].
41. Abraham AM, Lonkar SP, Pillai VV, Alhassan SM. Three-dimensional MoS_2 nanodot-impregnated nickel foam electrodes for high-performance supercapacitor applications. ACS Omega. 2020;5(20):11721–9. [CrossRef].
42. Gong Y, Wan J, Zhou P, Wang X, Chen J, Xu K. Oxygen and nitrogen-enriched hierarchical MoS_2 nanospheres decorated cornstalk-derived activated carbon for electrocatalytic degradation and supercapacitors. Mater Sci Semicond Process. 2021;123:105533. [CrossRef].
43. Yuan K, Zhuang X, Hu T, Shi L, Sfaelou S, Polnick U, et al. 2D heterostructures derived from MoS_2-templated, cobalt-containing conjugated microporous polymer sandwiches for the oxygen reduction reaction and electrochemical energy storage. ChemElectroChem. 2017;4(3):709–15. [CrossRef].
44. da Silveira Firmiano EG, Rabelo AC, Dalmaschio CJ, Pinheiro AN, Pereira EC, Schreiner WH, et al. Supercapacitor electrodes obtained by directly bonding 2D MoS_2 on reduced graphene oxide. Adv Energy Mater. 2014;4(6):1301380. [CrossRef].
45. Singh A, Iqbal M, Hazra KS, Mahapatra SK. High-energy-density quasi-solid-state supercapacitor with a MoS_2@FeS_2 core–shell heterostructure as an advance electrode material. Energy Fuels. 2024;38(5):4666–75. [CrossRef].
46. Giannozzi P, Andreussi O, Brumme T, Bunau O, Nardelli MB, Calandra M, et al. Advanced capabilities for materials modelling with Quantum ESPRESSO. J Phys Condens Matter. 2017;29(46):465901. [CrossRef].
47. Perdew J, Burke K, Ernzerhof M. Generalized gradient approximation made simple. Phys Rev Lett. 1996;77(18):3865–8. [CrossRef].
48. Hashemi A, Peljo P, Laasonen K. Understanding electron transfer reactions using constrained density functional theory: Complications due to surface interactions. J Phys Chem C Nanomater Interfaces. 2023;127(7):3398–407. [CrossRef].
49. Sruthi T, Tarafder K. Enhancement of quantum capacitance by chemical modification of graphene supercapacitor electrodes: A study by first principles. Bull Mater Sci. 2019;42(6):257. [CrossRef].
50. Dröscher S, Roulleau P, Molitor F, Studerus P, Stampfer C, Ensslin K, et al. Quantum capacitance and density of states of graphene. Appl Phys Lett. 2010;96(15):152104. [CrossRef].
51. Li P, Jiao Y, Huang J, Chen S. Electric double layer effects in electrocatalysis: Insights from *ab initio* simulation and hierarchical continuum modeling. JACS Au. 2023;3(10):2640–59. [CrossRef].